Time Series Scattering Power Decomposition Using Ensemble Average in Temporal–Spatial Domains: Application to Forest Disturbance Detection

Ryu Sugimoto, *Member, IEEE*, Ryo Natsuaki, *Senior Member, IEEE*, Ryosuke Nakamura, Chiaki Tsutsumi, and Yoshio Yamaguchi, *Life Fellow, IEEE*

***Abstract*— This letter proposes a novel synthetic aperture radar (SAR) time series analysis method based on the scattering power decomposition algorithm with a reasonable ensemble average in both temporal and spatial domains. We reveal that the ensemble average is effective not only in the spatial domain but also in the temporal–spatial domains in the scattering power decomposition. That is, if we extend the ensemble average window in the temporal domain, the proposed method can accurately achieve volume scattering power with a higher spatial resolution than conventional approaches. The precise volume scattering power serves accurate forest monitoring. As an application, we performed forest disturbance detection in the Amazon rainforest using Sentinel-1 time series data. The proposed method detected the disturbances earlier, in less than 2 months, compared to other methods that take about 3 months.**

***Index Terms*— Dual polarization, forest disturbance detection, scattering power decomposition, Sentinel-1, time series analysis, tropical forests.**

I. Introduction

POLARIMETRIC synthetic aperture radar (SAR) data preserve the dielectric properties and structures of scatterers, and they can be analyzed using various scattering power decomposition algorithms [1], [2]. However, these decomposition algorithms have limited applications owing to the infrequent acquisition of polarimetric SAR data. Thus, the scattering power decomposition algorithm has been extended to apply to dual-polarization data [3]. Since dual-polarization data are acquired more frequently than full-polarimetric SAR data, the analysis using time series data can be applied to land-use and land-cover classification, object change detection, and so on.

Most studies of changes in the tropical rainforests have focused on the causes and effects of deforestation. About 38% of the remaining forests in the Amazon are estimated to be degraded [4]. Thus, the detection of disturbances with less-intensity change in rainforest plays a crucial role in mitigating greenhouse gas emissions. Even though several deforestation detection systems have been applied operationally, detecting forest disturbances with less-intensity change remains a challenging task. For example, the conventional method using PALSAR-2 ScanSAR time series data, which is applied to the deforestation detection system, failed to detect disturbances with a logging intensity of about 20 m^3ha^{-1} in Saraca region of Brazil [5]. In the forest disturbance alert system using Sentinel-1 time series data, called radar for detecting deforestation (RADD) [6], it takes time to detect disturbances that appear similar to undisturbed forest on the radar image due to remaining woody debris. Furthermore, other methods using Sentinel-1 time series data took about 3 months to detect forest disturbances with a logging intensity of $\sim$30 m^3ha^{-1} or where trees remain after logging [7], [8].

In this study, to obtain the volume scattering power with the accurate and high spatial resolution, we propose a novel time series scattering power decomposition algorithm that extends the ensemble average window in both temporal and spatial domains. We then apply the method to Sentinel-1 C-band time series data for disturbance detection in the Amazon rainforest. With respect to the disturbance in this study, we define two levels. One is namely moderate disturbance with less-intensity change, such as the area where trees and/or undergrowth remain after logging, as shown in Fig. 1. In these areas, the intensity changes in the C-band SAR data are less than the range of the annual variability. The other is the high disturbance, defined as clear cutting such as deforestation.

The remaining sections of this letter are structured as follows. The proposed method is described in detail in Section II. The dataset and approach using the proposed method for forest disturbance detection are described in Section III. The experimental validation results are detailed in Section IV. The proposed method is compared with other time series analysis methods in Section V. Section VI presents the conclusion.

II. Time Series Scattering Power Decomposition

The scattering power decomposition algorithms offer superior target recognition, and many researchers have applied these algorithms to forest monitoring [9], [10], [11]. Recently, the application of these algorithms has been extended to dual-

Manuscript received 30 September 2023; revised 14 November 2023; accepted 16 December 2023. Date of publication 22 December 2023; date of current version 4 January 2024. This work was supported by the New Energy and Industrial Technology Development Organization (NEDO) under Project JPNP20006. *(Corresponding author: Ryu Sugimoto.)*

Ryu Sugimoto, Ryosuke Nakamura, and Chiaki Tsutsumi are with the Digital Architecture Research Center, National Institute of Advanced Industrial Science and Technology, Tokyo 135-0064, Japan (e-mail: sugimoto.ryu@aist.go.jp).

Ryo Natsuaki is with the Department of Electrical Engineering and Information Systems, The University of Tokyo, Tokyo 113-8656, Japan.

Yoshio Yamaguchi is with the Faculty of Engineering, Niigata University, Niigata 950-2181, Japan.

Digital Object Identifier 10.1109/LGRS.2023.3346378

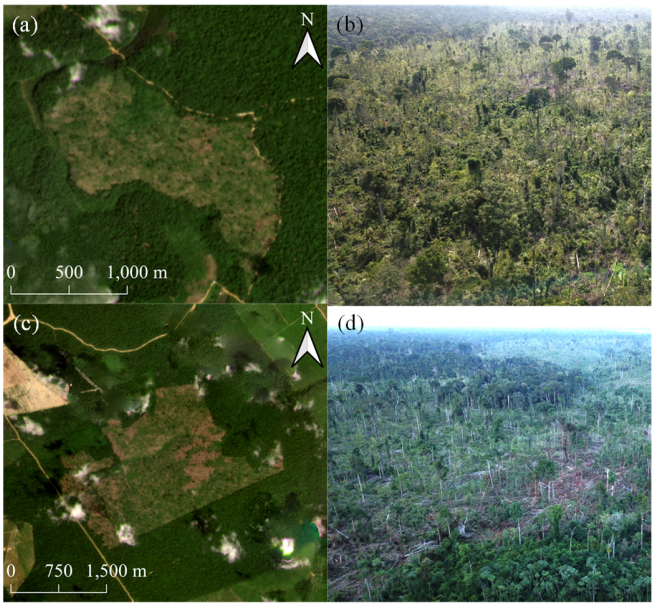

Fig. 1. Moderate disturbance at (a) and (b) site A1 and (c) and (d) site A2. (a) and (c) Mosaic images acquired by Planet/Dove in December 2021. (b) and (d) Drone image of the sites acquired in February 2022.

polarization data, so that they can be applied to more SAR data, as shown in the following [3]:

$$\langle [C2] \rangle = \begin{bmatrix} \langle C_{11} \rangle & \langle C_{12} \rangle \\ \langle C_{12}^* \rangle & \langle C_{22} \rangle \end{bmatrix} = P_g \begin{bmatrix} 1 & 0 \\ 0 & 0 \end{bmatrix} + \frac{P_v}{4} \begin{bmatrix} 3 & 0 \\ 0 & 1 \end{bmatrix} + \frac{P_h}{2} \begin{bmatrix} 1 & j \\ -j & 1 \end{bmatrix} \quad (1)$$

where $\langle [C2] \rangle$ denotes a 2×2 scattering covariance matrix with an ensemble average, and $*$ denotes complex conjugation. P_g, P_v, and P_h denote ground scattering, volume scattering, and helix scattering powers, respectively.

Conventionally, the ensemble average has been considered only for the spatial domain as follows:

$$\langle [C2] \rangle = \frac{1}{N_s} \sum_{i}^{N_s} [C2_i] \quad (2)$$

where N_s denotes the number of samples in the spatial domain. Assuming that the dielectric properties and structures of the scatterers change little over time or that the changes in scattering due to events, such as deforestation or seasonal variations, are consistent within the specific temporal window (i.e., the vegetation will not recover for months, resulting in a consistent scattering mechanism in most of the postlogging images), the ensemble average for the abundant dual-polarization data is extended to the temporal domain. A temporal intensity filter has been proposed to preserve strong scatterers in an image window [12], but it is not suitable for the scattering power decomposition and cannot handle complex correlations. Since the ensemble average in the scattering power decomposition serves to extract the statistical properties of the scatterers in an image window, we extend the ensemble average in the temporal–spatial domains as follows:

TABLE I

COMPONENTS OF THE COVARIANCE MATRIX USING (3) WITH $N_s = 20$ AND $N_t = 1$ OR 8 USING SENTINEL-1 TIME SERIES DATA IN THE SAN FRANCISCO ON JANUARY 21–APRIL 27, 2019. U: URBAN AREAS, B: BARE GROUND, AND TU: URBAN AREAS TILTED WITH RESPECT TO THE RADAR ILLUMINATION

LULC	N_t	$\langle C_{11} \rangle$ (%)	$\langle C_{22} \rangle$ (%)	$\lvert\langle C_{12} \rangle\rvert$ (%)
U	1	98.2±2.55	1.79±2.55	4.27±2.78
U	8	98.1±2.30	1.92±2.30	3.24±2.08
B	1	82.8±8.66	17.2±8.66	10.3±5.67
B	8	82.4±3.96	17.6±3.96	4.28±2.20
TU	1	76.8±10.1	23.2±10.1	13.4±7.11
TU	8	76.2±6.70	23.8±6.70	8.53±5.28

$$\langle [C2] \rangle = \frac{1}{N_t N_s} \sum_{j=1}^{N_t} \sum_{i=1}^{N_s} [C2_{i,j}] = \frac{1}{N_t N_s} \sum_{j=1}^{N_t} \sum_{i=1}^{N_s} \begin{bmatrix} \left| S_{\text{co-pol}_{i,j}} \right|^2 & S_{\text{co-pol}_{i,j}} S_{x-\text{pol}_{i,j}}^* \\ S_{x-\text{pol}_{i,j}} S_{\text{co-pol}_{i,j}}^* & \left| S_{x-\text{pol}_{i,j}} \right|^2 \end{bmatrix} \quad (3)$$

where N_t denotes the number of samples in the temporal domain, i.e., the number of images. $S_{\text{co-pol}}$ and $S_{x-\text{pol}}$ indicate the co- and cross-pol (S_{HH} and S_{HV} or S_{VV} and S_{VH}) components of the scattering matrix. The diagonal components in (3) represent the averaged power of the co- and cross-polarization, respectively. Also, the off-diagonal component in (3) represents the averaged complex correlation between the co- and cross-polarization. Table I shows an example of typical polarimetric features and their dependence on N_t derived from Sentinel-1 data in San Francisco, USA. In the urban area and the bare ground where the co-polarization scattering occurs, there is less change in the covariance matrix even when the ensemble average includes the temporal domain. The results suggest that in the C-band SAR data, the relationship between co- and cross-polarization of these scatterers is stable over temporal variations, such as rainfall. On the other hand, both cross-polarization scattering and complex correlation occur in the natural distributed objects and in the urban areas tilted with respect to the radar illumination. Scattering in the latter area is stable and unaffected by the time series ensemble average. For the natural distributed objects, such as natural vegetation, the complex correlation is close to zero when using a larger window in the spatial domain due to the phase from randomly distributed scatterers in the vegetation, i.e., $\langle S_{HH} S_{HV}^* \rangle \simeq 0$ and $\langle S_{VV} S_{VH}^* \rangle \simeq 0$. Such properties are called the reflection symmetry condition and lead to obtaining the covariance matrix of the volume scattering model [10]. If the ensemble-averaged samples can be obtained in both temporal and spatial domains, N_s can be smaller than that for the spatial domain only. Thus, the volume scattering power can be analyzed with a higher spatial resolution under the reflection symmetry condition. Although there are several factors that cause the temporal variation in natural vegetation, the randomness of the scatterer distribution cannot be altered, and natural

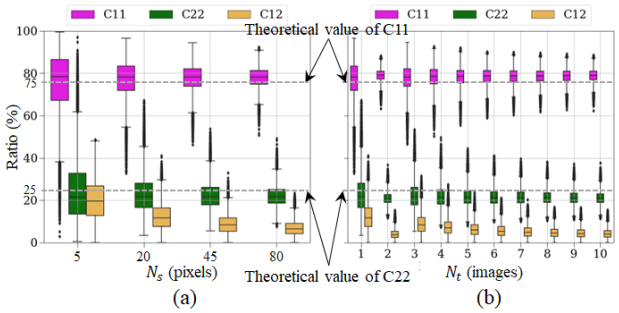

Fig. 2. Box plots of the components of the covariance matrix generated from grassland in Altamira using (a) (2) with different N_s and (b) (3) with different N_t and $N_s = 20$.

vegetation would be assumed to be a natural distributed object even in the temporal domain. For example, wind conditions change from moment to moment, causing the branches and leaves to sway randomly to the SAR sensor. Even with rainfall, the distribution of branches and leaves also remains random.

Fig. 2 shows the components of the covariance matrix generated from grassland using (2) and (3). Here, we used ten Sentinel-1 data acquired at Altamira in Brazil between May 6 and August 22, 2021. The N_s values of 5, 20, 45, and 80, which correspond to the spatial window sizes of 1 $\times$ 5, 2 $\times$ 10, 3 $\times$ 15, and 4 $\times$ 20 pixels in the azimuth and range directions, respectively, are used in (2). In (3), N_t is used from 1 to 10, while N_s is fixed at 20. As shown in (1), the theoretical values of $\langle C_{11}\rangle$, $\langle C_{22}\rangle$, and $|\langle C_{12}\rangle|$ in the volume scattering model are derived to be 75%, 25%, and 0% of total power, respectively. The larger N_s achieves the ratio of components close to theoretical values, as shown in Fig. 2(a). For example, $\langle C_{11}\rangle$, $\langle C_{22}\rangle$, and $|\langle C_{12}\rangle|$ with $N_s = 80$ indicate an average and standard deviation of 77.9% $\pm$ 4.86%, 22.1% $\pm$ 4.86%, and 6.89% $\pm$ 3.53%, respectively. The difference from the theoretical values in (1) can be attributed to the short wavelength; C-band SAR cannot penetrate deeply into the vegetation due to their short wavelength and the volume scattering power generated from the vegetation is not dominant component [13]. As shown in Fig. 2(b), increasing N_t and increasing N_s have similar effects. When using (3) with $N_s = 20$, $\langle C_{11}\rangle$, $\langle C_{22}\rangle$, and $|\langle C_{12}\rangle|$ start from 77.1% $\pm$ 8.73%, 22.9% $\pm$ 8.73%, and 12.3% $\pm$ 6.18% with $N_t = 1$. Then, they show 78.2% $\pm$ 4.38%, 21.8% $\pm$ 4.38%, and 6.38% $\pm$ 3.29% with $N_t = 4$, which are equivalent to those obtained using (2) with $N_s = 80$. Therefore, in natural vegetation, time series ensemble average with small N_s can realize the reflection symmetry condition with specific N_t and analyze the volume scattering power with an accurate and high spatial resolution. The components of the covariance matrix finally converge to 78.7% $\pm$ 3.20%, 21.3% $\pm$ 3.20%, and 4.52% $\pm$ 2.35% with $N_t = 8$. This property also holds true for the covariance matrix of forests as well.

The time series scattering power decomposition, i.e., applying the covariance matrix in (3) to the scattering power decomposition algorithm in (1), yields three scattering powers with high spatial resolution. Since the time series scattering power decomposition is frequency-independent, it is applicable to abundant SAR data with a few weeks repeat cycle, such as Sentinel-1 (C-band SAR), NISAR (L-/S-band SAR), and ALOS-4 (L-band SAR) data.

III. Application to Forest Disturbance Detection Using Sentinel-1 Data

A. Dataset

In this study, two time series of Sentinel-1A single look complex data are used. One is the data acquired between March and December 2021 covering moderate disturbance sites, as shown in Fig. 1, namely, site A1 at 51.8 W and 2.6 S and site A2 at 51.7 W and 2.9 S. The other is the data acquired between April and November 2022 covering 51.0–52.0 W and 2.0–3.0 S. The moderate disturbance sites, where are included in the 2021 time series data, are located in Altamira, Brazil, and were confirmed by optical satellite images to have begun in September 2021. A field survey was conducted there by the Japan International Cooperation Agency (JICA) in February 2022. These data, along with forest and nonforest samples from around the site, were used to study the change in scattering power with disturbance. For the time series data in 2022, the reference data were created by visual interpretation using the Planet biannual base map from the Norway's International Climate and Forests Initiative satellite data program. The reference data consist of 504 polygons representing the moderate (231 polygons) and high (273 polygons) disturbances detected in August and September 2022. They were used to validate the accuracy of forest disturbance detection.

B. Disturbance Detection

Unlike in deforestation, in moderate disturbances, the remaining trees and undergrowth contribute to the backscatter, resulting in less variability in the backscatter before and after the event. Thus, it is difficult to detect moderate disturbances from the change in the scattering power. By using the proposed method, the total scattering power image generated from Sentinel-1A time series data showed forest textures with spatial patterns similar to the canopy structure and also reduced the contrast of both sites A1 and A2 compared to that of the forest. Therefore, the proposed method can extract the texture difference between forest and moderate disturbance due to its high spatial resolution, and the following condition can be used to detect the moderate disturbance

$$\text{Texture}_{\text{pre-event}} > \alpha \cap \text{Texture}_{\text{postevent}} \leq \alpha \tag{4}$$

where "pre-event" and "postevent" denote before and after the forest disturbance, respectively. α denotes an empirical threshold and is determined by analyzing the texture at both sites A1 and A2. In this study, the contrast of the gray-level co-occurrence matrix is used as texture. Other textures, such as correlation, homogeneity, and dissimilarity, may also contribute to disturbance detection. The combining textures for disturbance detection will be considered in future work.

To determine the threshold α in (4), disturbances initiated in September 2021 at both sites A1 and A2 were analyzed

using the combination of N_s, N_t, and texture window. In this analysis, N_s of 20, 45, and 80, and the texture windows of 3×3, 5×5, 7×7, and 9×9 were used. We also used $N_t = 8$, i.e., eight images each in the pre- and postevent periods, and the following four image periods in 2021 were used: P1 is March 19–June 11 (pre-event) and June 23–September 27 (postevent); P2 is April 12–July 5 and July 17–October 21; P3 is May 18–August 10 and August 22–November 26; and P4 is June 11–September 3 and September 27–December 20. For each of the 48 combinations of N_s, N_t, and texture window, the threshold α was increased from 0.1 to 30 in 0.1 increments to determine the optimal value for disturbance detection.

We demonstrated the proposed approach with the reference data as follows. First, the scattering powers were calculated separately before and after the event using (1) and (3) with Sentinel-1A time series data stacked on a common grid, and the contrast of total scattering power was derived using the texture window. Then, the vegetation pixels satisfying (4) with optimal α were detected as disturbances. Note that the pixels with a volume scattering power greater than 0.05 in the pre-event were considered as vegetation pixels. Finally, the disturbance map was geocoded for comparison with the reference data. For this comparison, N_t was set to eight images for the image period abbreviated as P5, April 19–August 17 (pre-event) and August 29–November 21 (postevent) in 2022. In addition, we set N_s to 20 and texture windows to 3×3, and the minimum detection size was set to 2.0 ha as in [5].

IV. Results

The α values of 7.5, 6.7, 5.0, and 5.4 for image periods P1–P4 were found to be the optimal when using the $N_s = 20$ and 3×3 texture windows at site A1. When applying these settings, the disturbance map in image period P3 is shown in Fig. 3 and the disturbance detection accuracy is shown in Fig. 4. As the number of images affected by the disturbance in the postevent image increases, the texture of the disturbance area decreases compared to the forest, and the number of detected pixels increases. The number of detected pixels then decreases as the number of such images in the pre-event image increases. The RADD failed to detect disturbances in both sites A1 and A2 even in December 2021. In contrast, the proposed method detected 20% of the disturbances as of October and about 40% within 2 months of their occurrence in both sites. In terms of texture window, increasing it reduces the omission error, while decreasing it reduces the commission error. A smaller N_s reduces both errors.

For the comparison with the reference data, smaller N_s and texture windows were used to demonstrate forest disturbance detection with low commission error. No salt-and-pepper noise was found in the detection result. Table II shows the accuracy based on the reference data when using $N_s = 20$, 3×3 texture windows, and α of 6.7. The method can detect the moderate disturbance with reasonable accuracy ~2 months after its occurrence. When the high disturbance is added to the reference data, UA of >70% achieves, and PA decreases due to the failure to detect the small disturbance

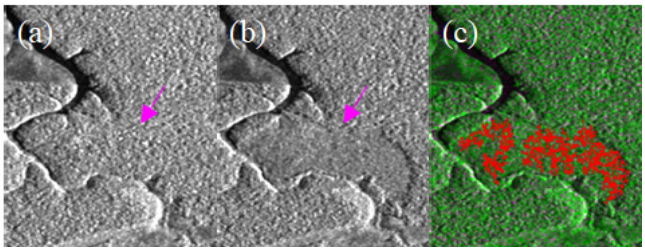

Fig. 3. Disturbance map at site A1 in image period P3. Images of the total scattering power in (a) pre-event and (b) postevent. The magenta arrow indicates the disturbance area. (c) Disturbance map in red overlays on the time series scattering power decomposition RGB images.

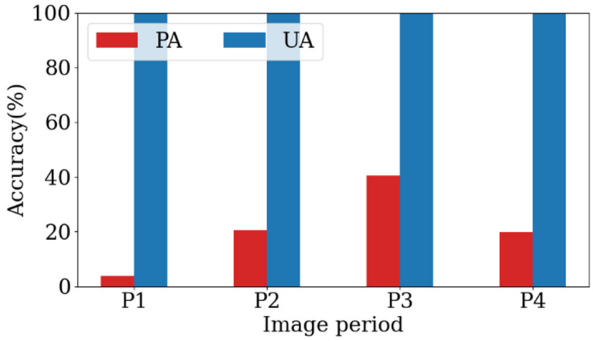

Fig. 4. User's and producer's accuracy (UA and PA) at site A1 using the optimal α, $N_s = 20$, and 3×3 texture windows.

TABLE II
UA and PA Based on the Reference Data Using the Optimal α, $N_s = 20$, and 3×3 Texture Windows

Image period	Disturbance level in reference data	UA (%)	PA (%)
P5	Moderate	46.6	70.6
	Moderate and High	71.4	59.5

(~10 ha). In addition, about 30% of the commission error may not be a detection error because it includes the detection of changes from moderate to high disturbance and of the moderate disturbance that occurred after September.

V. Discussion

The time series analysis method of the scattering power decomposition algorithm was applied to detect forest disturbance using Sentinel-1A time series data. In [3] and [10], the moderate disturbance could not be detected because the L-band SAR data used were acquired less frequently than the Sentinel-1 data and only the ensemble average in the spatial domain was available. Using the ensemble average window in the temporal–spatial domains, the scattering power with accurate and high spatial resolution could detect even moderate disturbances ~2 months after their occurrence. In this regard, a previous study proposed a change detection algorithm using temporally stacked interferometric coherence (TSIC) with a small spatial window [14]. TSIC detects the building damage by using the coherence between pre- and postevents, assuming that in multiple interferometric pairs, the scatterers as targets are stable over temporal decorrelation. In C-band SAR data,

TSIC cannot be applied to forest disturbance detection because the vegetation is affected by temporal decorrelation. In contrast, the proposed method can be applied to forest monitoring using C-band SAR time series data because the method does not require such an assumption.

Another study proposed a time-averaged method to classify forest species, and this method averages the scattering powers generated from multitemporal quad-polarization data [11]. Since the time-averaged method does not consider the correlation between co- and cross-polarization data in the temporal domain, it requires a large spatial window size to drive the reflection symmetry condition, whereas the proposed method can obtain the scattering powers with accurate and high spatial resolution by considering the correlation in the temporal domain. The texture of intensity change in SAR data was available for the forest disturbance detection in [15] and [16]. In areas containing both unlogged and logged forest pixels, the intensity changes exhibit light and dark tonal textures. However, if trees and undergrowth remain, as shown in Fig. 1, the C-band radio waves cannot penetrate to the ground, so no significant intensity changes are expected to appear. Because the proposed method can show the difference between forest and grassland textures with high spatial resolution, it is useful for detecting moderate disturbances.

The proposed decomposition method is suitable for SAR imagery acquired at various frequency bands, such as L/C, but its meaningfulness depends on observing scattering stability over the chosen temporal window. Future work will address how long this assumption holds. A crucial limitation arises when a significant change in the scattering mechanism occurs within the temporal window. In this situation, the co- and cross-polarization components are somewhat meaningful because they represent the averaged power, but the averaged complex correlation makes little sense. For the volume scattering objects (e.g., natural vegetation and sea ice), the volume scattering power may be overestimated if the reflection symmetry condition is not properly satisfied. The averaged power of the co- and cross-polarization can be one of the useful indicators to assess if the scattering mechanism remains relatively constant over time.

VI. Conclusion

In this letter, we proposed a time series scattering power decomposition using the ensemble average in the temporal–spatial domains. The proposed method extracts accurate volume scattering power and forest texture due to its high spatial resolution. As a result, the proposed method can detect the moderate disturbance in the rainforest with UA of >70% in less than 2 months, whereas other methods require about 3 months. Here, only Sentinel-1A data with 12-day repeat cycles were used. Time series SAR data with different wavelengths will be available in future. The use of these data may further reduce the time lag in detecting forest disturbances.

Acknowledgment

The drone images and the reference data at Altamira were provided by JICA-led Project MORI (project for improving control of illegal deforestation through advanced SAR and AI technologies in the Brazilian Amazon).

References

[1] G. Singh, Y. Yamaguchi, and S.-E. Park, "General four-component scattering power decomposition with unitary transformation of coherency matrix," *IEEE Trans. Geosci. Remote Sens.*, vol. 51, no. 5, pp. 3014–3022, May 2013, doi: 10.1109/TGRS.2012.2212446.

[2] G. Singh and Y. Yamaguchi, "Model-based six-component scattering matrix power decomposition," *IEEE Trans. Geosci. Remote Sens.*, vol. 56, no. 10, pp. 5687–5704, Oct. 2018, doi: 10.1109/TGRS.2018.2824322.

[3] R. Sugimoto, R. Nakamura, C. Tsutsumi, and Y. Yamaguchi, "Extension of scattering power decomposition to dual-polarization data for tropical forest monitoring," *Remote Sens.*, vol. 15, no. 3, p. 839, Feb. 2023, doi: 10.3390/rs15030839.

[4] D. M. Lapola et al., "The drivers and impacts of Amazon forest degradation," *Science*, vol. 379, no. 6630, Jan. 2023, Art. no. eabp8622, doi: 10.1126/science.abp8622.

[5] M. Watanabe, C. N. Koyama, M. Hayashi, I. Nagatani, T. Tadono, and M. Shimada, "Refined algorithm for forest early warning system with ALOS-2/PALSAR-2 ScanSAR data in tropical forest regions," *Remote Sens. Environ.*, vol. 265, Nov. 2021, Art. no. 112643, doi: 10.1016/j.rse.2021.112643.

[6] J. Reiche et al., "Forest disturbance alerts for the Congo basin using Sentinel-1," *Environ. Res. Lett.*, vol. 16, no. 2, Jan. 2021, Art. no. 024005, doi: 10.1088/1748-9326/abd0a8.

[7] M. G. Hethcoat, J. M. B. Carreiras, D. P. Edwards, R. G. Bryant, and S. Quegan, "Detecting tropical selective logging with C-band SAR data may require a time series approach," *Remote Sens. Environ.*, vol. 259, Jun. 2021, Art. no. 112411, doi: 10.1016/j.rse.2021.112411.

[8] E. L. Bullock et al., "Timeliness in forest change monitoring: A new assessment framework demonstrated using Sentinel-1 and a continuous change detection algorithm," *Remote Sens. Environ.*, vol. 276, Jul. 2022, Art. no. 113043, doi: 10.1016/j.rse.2022.113043.

[9] N. C. Wiederkehr et al., "Discriminating forest successional stages, forest degradation, and land use in central Amazon using ALOS/PALSAR-2 full-polarimetric data," *Remote Sens.*, vol. 12, no. 21, p. 3512, Oct. 2020, doi: 10.3390/rs12213512.

[10] R. Sugimoto, S. Kato, R. Nakamura, C. Tsutsumi, and Y. Yamaguchi, "Deforestation detection using scattering power decomposition and optimal averaging of volume scattering power in tropical rainforest regions," *Remote Sens. Environ.*, vol. 275, Jun. 2022, Art. no. 113018, doi: 10.1016/j.rse.2022.113018.

[11] Priyanka et al., "Forest plantation species classification using full-pol-time-averaged SAR scattering powers," *Remote Sens. Appl., Soc. Environ.*, vol. 29, Jan. 2023, Art. no. 100924, doi: 10.1016/j.rsase.2023.100924.

[12] S. Quegan and J. J. Yu, "Filtering of multichannel SAR images," *IEEE Trans. Geosci. Remote Sens.*, vol. 39, no. 11, pp. 2373–2379, Nov. 2001, doi: 10.1109/36.964973.

[13] R. Sugimoto, R. Nakamura, C. Tsutsumi, and Y. Yamaguchi, "Scattering power decomposition of dual-polarization SAR data: Application to PALSAR-2 and Sentinel-1 data," in *Proc. URSI GASS*, Sapporo, Japan, Aug. 2023, pp. 1–3. [Online]. Available: https://doi.org/10.23919/URSIGASS57860.2023.10265560

[14] R. Natsuaki, R. Sugimoto, M. Shimada, C. Tsutsumi, and R. Nakamura, "Urban damage detection using temporally stacked synthetic aperture radar interferometric coherence," in *Proc. IGARSS*, Pasadena, CA, USA, Jul. 2023, pp. 1991–1993. [Online]. Available: https://doi.org/10.1109/IGARSS52108.2023.10282496

[15] D. Hoekman et al., "Wide-area near-real-time monitoring of tropical forest degradation and deforestation using Sentinel-1," *Remote Sens.*, vol. 12, no. 19, p. 3263, Oct. 2020, doi: 10.3390/rs12193263.

[16] O. Antropov, Y. Rauste, J. Praks, F. M. Seifert, and T. Häme, "Mapping forest disturbance due to selective logging in the Congo basin with RADARSAT-2 time series," *Remote Sens.*, vol. 13, no. 4, p. 740, Feb. 2021, doi: 10.3390/rs13040740.